

Kirigami and Mogul-Patterned Ultra-Stretchable High-Performance ZnO Nanowires-Based Photodetector

Yogeenth Kumaresan, Guanbo Min, Abhishek Singh Dahiya, Ammara Ejaz, Dhayalan Shakthivel, and Ravinder Dahiya*

Wearable UV photodetectors (PDs) have attracted interest recently for detection of excess exposure of the skin to the UV radiation. Despite numerous advances made in this direction, many challenges remain, particularly in terms of device reliability under extreme mechanical deformations simultaneously and self-powering, etc. Herein, a self-powered stretchable PD developed with kirigami-inspired honeycomb-patterned zinc oxide (ZnO) nanowires (NWs) and coupled with a triboelectric nanogenerator (TENG) is presented. After studying in detail the influence of ZnO NWs dispersion medium and metal-ZnO NWs contacts, a novel fabrication approach employing the structural engineering on NWs-elastomer composite is used to achieve high stretchability. The fabricated ZnO NWs-based UV PDs, embedded inside kirigami-inspired honeycomb-patterned elastomeric substrate, exhibit unprecedented stretchability (up to 125%) and high-performance with photo/dark current ratio of $\approx 5 \times 10^5$, responsivity of $\approx 54 \text{ A W}^{-1}$, and a fast recovery time of 100 ms. Further, the stretchable PD is coupled with flexible TENGs to demonstrate a self-powered system for potential application in real-time UV radiation monitoring using advanced wearable healthcare technology.

1. Introduction

UV radiations have significant health benefits including enabling the production of Vitamin D, which is needed for stronger bones and muscles.^[1] However, for desired benefits it must be controlled as, excessive exposure to UV radiation could cause skin cancer,^[2] eye damage,^[3] accelerate skin aging process.^[4] The impact is beyond healthcare, as the excessive exposure to UV radiation could adversely affect the over-cultivation of lands, crops, and buildings.^[1a] The amount of UV radiation on earth surface varies due to the decline in the UV protective stratospheric ozone layer. The seasonal UV intensity fluctuations and diverse geographical locations make UV detection quite chal-

lenging.^[5] Therefore, highly stretchable photodetector (PD) devices having the potential to attach on nonplanar surfaces such as clothes or skin to endure body motions are highly desirable for real-time monitoring of UV radiation under diverse environmental conditions.^[6] Additionally, for real-time operation the self-powering of myriad sensors and electronics on wearable systems is desirable.^[7]

Enormous efforts have been made to achieve stretchable UV PDs to go beyond the existing silicon-based rigid electronics.^[8] These solution typically adopt the techniques that have developed for stretchable and wearable electronics, which has gained significant interest in recent years because of the need for electronics in flexible form factors in a wide range of applications.^[9] Few examples include mobile health monitoring through sensory skin patches,^[10] communication through wearable devices or foldable displays,^[8c,11]

safe robotic interaction through large area tactile skin, etc.^[12] On-going research efforts focus on the development of multi-modal wearables that can be easily integrated in clothing, wrist watches and bands, tattoo-like sensory skin patches (electronic-skin), etc.^[13] To this end, highly sensitive sensors with high stretchability and reliability are recommended for accurate and fast measurements during body movements.^[14]

The stretchable PDs are fabricated thus far either use novel structural device engineering^[8b,14a,15] or the nanowires (NWs)-elastomer nanocomposite by embedding the semiconducting NWs in the elastomeric material.^[8c,8d,8f,16] The former approach relies on the structural design of nonstretchable materials which includes the fabrication of PD through a conventional approach and transfer to the prestretched substrate to obtain a stretchable wavy pattern upon releasing the prestrain. For example, a stretchable graphene PD was fabricated by transferring graphene layer to a prestretched polydimethylsiloxane (PDMS) membrane to achieve wavy graphene with enhanced stretchability.^[17] Similarly, patterning the nonstretchable active materials such as InGaZnO and gold to stretchable geometries such as serpentine, zigzag, or honeycomb^[18] has been explored. Alternatively, stress-absorbing substrates, namely, mogul^[15] or kirigami^[8b] patterned substrates have been utilized to achieve stretchable PDs.^[8b,15] However, most of the PDs have limitations either in the device performance,^[8b,c,17] such as poor photocurrent ratio and slow response/recovery time or in the device

Y. Kumaresan, G. Min, A. S. Dahiya, A. Ejaz, D. Shakthivel, R. Dahiya
Bendable Electronics and Sensing Technologies (BEST) Group
University of Glasgow
Glasgow G12 8QQ, UK
E-mail: Ravinder.Dahiya@glasgow.ac.uk

 The ORCID identification number(s) for the author(s) of this article can be found under <https://doi.org/10.1002/admt.202100804>.

© 2021 The Authors. Advanced Materials Technologies published by Wiley-VCH GmbH. This is an open access article under the terms of the Creative Commons Attribution License, which permits use, distribution and reproduction in any medium, provided the original work is properly cited.

DOI: [10.1002/admt.202100804](https://doi.org/10.1002/admt.202100804)

Table 1. Performance comparison of ZnO NW-based photodetectors.

Contact electrode	Rise time	Decay time	Photocurrent ratio ($I_{\text{Photo}}/I_{\text{Dark}}$)	Responsivity [A W^{-1}]	Stretchability [%]	Ref.
Pd	NA	≈0.9 s	>10 ⁴	NA	No	[30a]
Carbon paste and In/Ag	21.5 s	10.5 s	10 ⁸	NA	No	[8a]
Au	≈10 s	≈230 s	>10	4.5	No	[8d]
Ag-NW	1.83 s	1.75 s	9780	4.16	No	[30b]
Cr/Au	>10 s	>30 s	NA	86	30%	[15]
Au@PVP nanofiber	90 s	46 s	1020	0.12 × 10 ⁻³	80%	[8b]
Ag-NW	0.8 s	1.6 s	>10 ²	10–30	60%	[8c]
Ag NW+Ag-Paste	≈0.2 s	≈0.1 s	5 × 10 ⁵	54	125%	This work

flexibility/stretchability (see the Table 1).^[8e,19] The fast response and recovery characteristics are crucial for optoelectronic and high-frequency applications.^[20] The slow response of PDs could be caused by charge traps and surface states and can be overcome by passivating the active material and/or by achieving a Schottky contact.^[21] Since embedding of NWs inside soft material enhances the overall stretchability and the structural engineering allows devices to have stable device performance, a combination of both the strategies together, i.e., embedding the NWs inside a patterned substrate, could yield high performance along with stable stretchable devices. Therefore, a systematic approach as shown in Figure S1 in the Supporting Information is crucial to obtain the high-performance of stretchable device over state-of-the-art devices reported so far (Table 1). For example, the semiconductor NW–NW interaction study provides an insight to tune the channel resistance; the semiconductor–metal interaction helps to understand the contact resistance; and the patterning helps to achieve stretchability without affecting the performance. Focusing only on single study or skipping some of the studies would not have been sufficient when it comes to obtaining both good performance and high stretchability. Herein, we have used this strategy to develop the ZnO NWs-based ultra-stretchable high-performance PD.

With ZnO NWs embedded in honeycomb-inspired kirigami and/or mogul-patterned PDMS (Figure 1), the presented UV PDs exhibit unprecedented stretchability (up to 125%) and stable and high performance with photo/dark current ratio of ≈5 × 10⁵, responsivity of ≈54 A W⁻¹, and a fast recovery time of 100 ms. To the best of our knowledge, the obtained stretchability is one of the best among the reported stretchable ZnO NW PDs (Table 1). The high-performance is obtained by optimizing two important factors: i) the ZnO NWs dispersion medium, namely, water, ethanol, and isopropanol (IPA); and ii) the contact electrodes including gold (Au), silver (Ag), and Ag NWs on ZnO NWs. We observed a fast switching behavior with full recovery in less than 100 ms, which is at least an order of magnitude better than previous reports (Table 1) and thus marks a significant improvement over the state of the art. Further, the presented UV PD was integrated with a flexible triboelectric nanogenerators (TENGs) device to achieve self-powered system suitable for the real-time health monitoring.^[7a,22] As a proof of concept, the stretchable PD coupled with flexible TENGs was connected to the light-emitting diode (LED) for real-time monitoring of UV radiation (Figure 1).

2. Result and Discussion

2.1. High-Performance Stretchable ZnO NW UV PDs

The performance optimization of ZnO NW PDs was conducted by investigating the influence of different ZnO NW's dispersion medium (Figure 2), and the role of various contact electrodes (Figure 3). The device fabrication scheme shown in Figure S1 in the Supporting Information was utilized to fabricate ZnO NW PD devices on polyvinyl chloride (PVC) substrate. For a planar ZnO NW PDs with a metal-semiconductor-metal structure, there are primarily two important components, i.e., semiconductor channel resistance (R_{CH}) and MS contact resistance (R_{C1} and R_{C2}), which play key role in defining the sensor performance.^[8a] These are schematically shown in Figure 2a. Equations (1) to (4) explain the influence of multiple nanowire junction resistance (Equation (3)) and metal-nanowire contact (Equation (4)) toward the photodetector performance (Equation (1))^[20b]

$$\Delta I \text{ (Photo to dark current)} = \frac{V}{R_{\text{dark}}} - \frac{V}{R_{\text{light}}} \quad (1)$$

$$R_{\text{dark}} \text{ or } R_{\text{light}} = R_{\text{c}} + R_{\text{CH}} \quad (2)$$

$$R_{\text{CH}} = R_{j1} + R_{j2} + R_{j3} \dots \dots \dots R_{jn} \quad (3)$$

$$R_{\text{c}} = R_{\text{C1(metal-nanowire junction 1)}} + R_{\text{C2(metal-nanowire junction 2)}} \quad (4)$$

here R_{dark} and R_{light} are the resistance of the device under dark and UV light; R_{c} is the contact resistance; and R_j is the nanowire–nanowire junction resistance. The systematic study on channel resistance, contact resistance, and stretchability as shown in Figure S1a in the Supporting Information were performed to obtain high-performance stretchable PD devices.

2.1.1. ZnO NW-ZnO NW Interaction on Channel Resistance of ZnO NW UV PDs

The channel resistance of the PD is investigated by studying the influence of ZnO NWs dispersion medium over the PD's performance. The three variant of PD devices were fabricated by dispersing 0.3 wt% ZnO NWs in three different solvents, namely, deionized (DI) water, ethanol, and IPA. The ZnO NW solutions were drop-casted on ≈175 μm thick PVC substrates

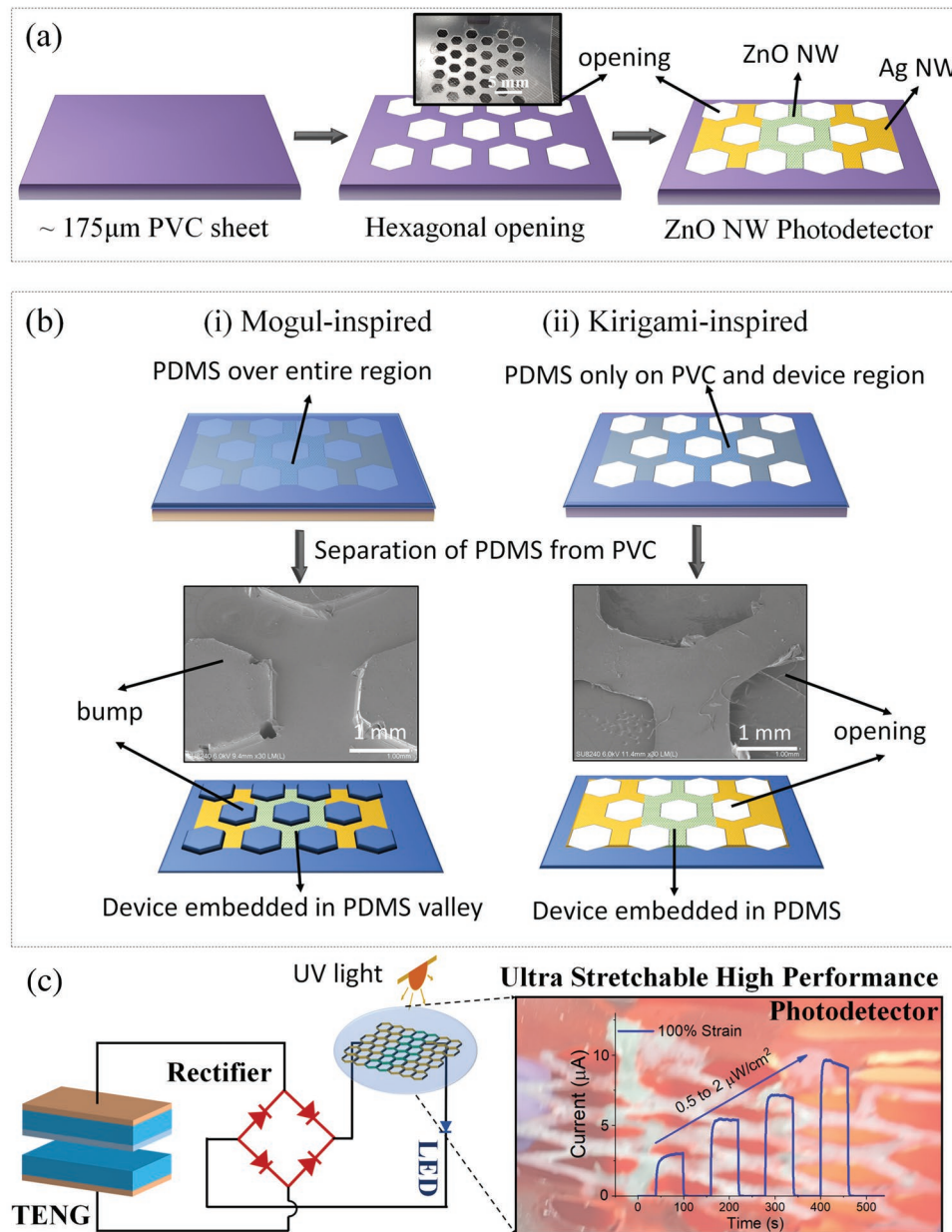


Figure 1. Schematic representation of the fabrication process for self-powered stretchable photodetector (PD): a) Fabrication of honeycomb-patterned ZnO NW PD on PVC substrate, a photographic image of honeycomb-patterned PVC substrate is shown in the inset; b) stretchable PD fabrication by embedding the ZnO NW PDs in honeycomb-patterned PDMS either as i) mogul-inspired pattern consists of bump and valley architecture (a cross-sectional scanning electron microscope (SEM) image of bump and valley-structured PDMS is shown in the inset) or ii) kirigami-inspired architecture (a cross-sectional SEM image of hexagonal opening is shown in the inset); and c) integration of stretchable photodetector with triboelectric nanogenerator (TENG) through LED light to monitor the UV light through the light intensity of LED. The optical image and time-resolved photoresponse of stretchable PD at 100% strain.

and annealed at 100 °C for 10 min. Sequentially, the PD's channels length (40 μm) and width (1 mm) were defined using the stencil lithography method. The silver metal of 80 nm thickness was deposited through the shadow mask using a thermal evaporation tool. A bias voltage of 2 V was applied to all three devices and the time-resolved photoresponse was measured by exposing them to 365 nm UV light by varying the intensity from 0.5 to 2.0 μW cm⁻². As shown in Figure 2c,d, an increase

in current level was observed for all the devices under UV illumination. The energy band diagrams for the device structure, in dark and UV light illumination, are also shown in Figure 2b. For a multiple NW network-based device (like in the present study), irrespective of the type of metal contacts, the interface gating effect due to multiple NW–NW interfaces/junctions plays dominant role in defining the device performance.^[8a] Accordingly, ZnO NWs form a highly resistive channel between

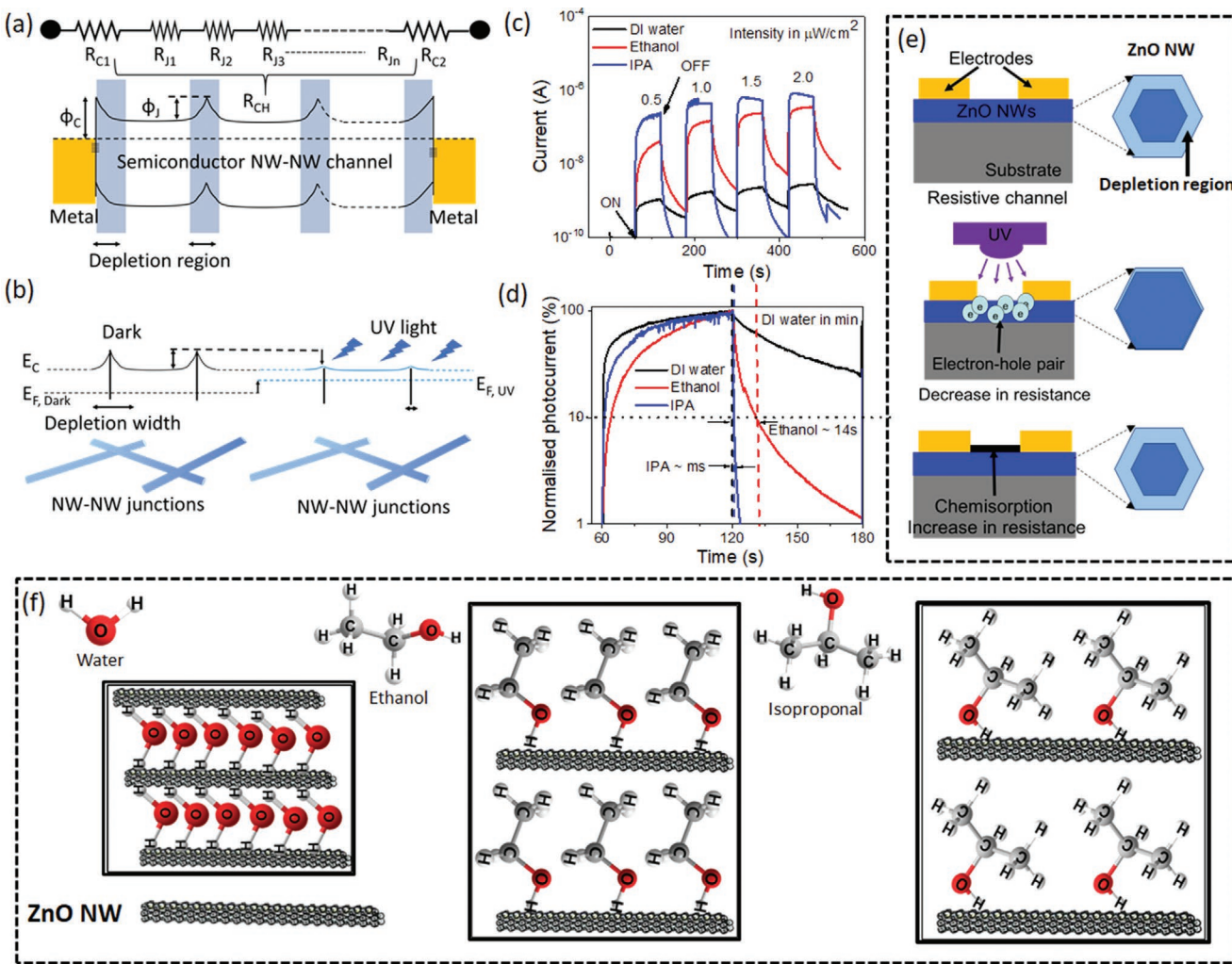


Figure 2. Role of ZnO NWs dispersed in three different solvents (DI water, ethanol, IPA) and their photodetector performance: a) Band diagram of metal-ZnO NWs network-metal UV PD with the series of contact and channel resistances; b) energy band diagram of NW network (channel region) under dark and UV light; c) the time-resolved photocurrent response under the UV (365) intensity varied from 0.5 to 2.0 $\mu\text{W cm}^{-2}$; d) the normalized photocurrent value in % with time highlighting the 90% recovery time; e) schematic of the working mechanism of ZnO NW photodetector; and f) the chemical structure of water, ethanol, and IPA and their interaction with ZnO NWs.

the contact electrodes under the absence of UV light (Figure 2e, top scheme) due to the low free charge density and the high NW–NW junction resistance (Equation (3)).^[23] Further, oxygen species available in the ambient conditions are chemisorbed on the surface of ZnO NWs and capture the free electrons from ZnO NWs (equation 5), resulting in the formation of a depletion region at the surface of NWs (Figure 2e).^[24] This results in an upward band bending near the surface and consequently, an electric barrier across the NW–NW interface is formed (Figure 2b). This barrier must be overcome to initiate the transport of charges



Accordingly, all three devices demonstrated negligible current under no UV illumination, as shown in Figure 2a. When the device was illuminated by 365 nm UV light, a large number of electron–hole pairs are generated as shown in Equation (6)

(as the exposed photon energy of 3.4 eV was sufficient to excite the electrons to the conduction band, leaving holes in the valence band (band gap of ZnO is 3.34 eV)). Following that the photogenerated holes migrate to the ZnO NWs surface and react with the chemisorbed oxygen ions, resulting in the desorption of chemisorbed oxygen ions and release of the captured free electrons (Equation (7))



This phenomenon has enriched free electrons in ZnO NWs and a consequent decrease in the surface depletion region width (Figure 2e, middle scheme). It is well known that the width of a depletion region is inversely proportional with the intrinsic carrier concentration in semiconductors.^[25] Hence, the barrier across the NW–NW interface decreases (Figure 2b) and

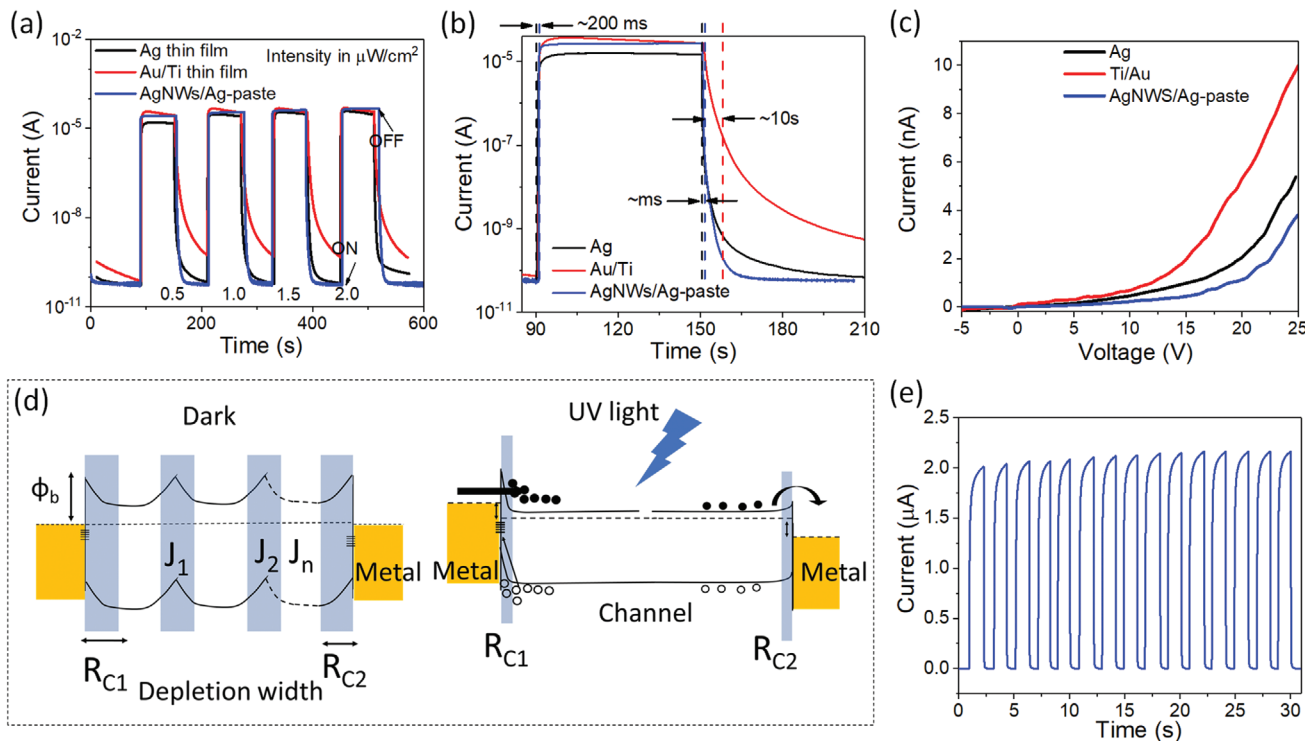


Figure 3. The effect of contact electrodes on photodetector performance: a) The time-resolved photocurrent response under the UV (365) intensity varied from 0.5 to 2.0 $\mu\text{W cm}^{-2}$; b) the magnified time-resolved photocurrent response highlighting the response and recovery time; c) current–voltage characteristics under dark state; d) energy band diagram of ZnO NW PD under dark and UV light in which reverse biased junction form R_{C1} depletion and forward biased junction forms the R_{C2} depletion width; and e) cyclic photoresponse with 1 s “on” and 1 s “off” for 15 cycles under the UV intensity of 0.35 $\mu\text{W cm}^{-2}$.

the flow of electrons is promoted. Accordingly, the current level increases on UV illumination, as shown in Figure 2c,d. Further, when UV illumination was turned off, recombination of electron-hole pairs results in the decrease of free carriers and the channel current level.

The rise and recovery time for the devices prepared via three different solvents show significant differences (Figure 2d). The possible reason could be the different mediums of ZnO NWs dispersion and their molecular structures.^[26] The molecular geometry of water, ethanol, and IPA are shown in Figure 2f. It can be seen from this figure that H_2O has a bent geometry with three possible interacting atoms to engage ZnO NWs. Ethanol also possesses a bent structure with two coordination sites to interact with ZnO NWs. However, IPA is secondary alcohol which is linked to a -OH group through two other carbon atoms. The presence of a highly electronegative atom (O) generates polarity in all molecules and provides a potential coordination site through physio- and chemisorption attractions or via H-bonding. On the other hand, in the case of ZnO, Zn and O atoms form a consecutive layered structure, the molecular geometry of H_2O will allow interaction of the ZnO NWs in all *a*, *b*, and *c*-axis of its wurtzite structure which will result in the agglomeration of ZnO NWs in the solution (Figure 2f). As a result, drop casted ZnO NWs are nonuniformly coated between the contact electrodes, leading to bundling of NWs together at some locations and empty spaces at the other (Figure S2a, Supporting Information). This phenomenon leads to a smaller

number of NWs between the contact electrodes that eventually decreases the photocurrent (Figure 2c). Likewise, the bundling of NWs together will reduce the effective outer surface area that is responsible for chemisorption and electron depletion (Figure S2f, Supporting Information).^[27] Therefore, ZnO NWs PD device obtained from water-based dispersion exhibits larger recovery time (>60 s). In the case of ethanol, O and H atoms are the potential physio- and chemisorption sites for the attachment of ZnO NWs while the opposite side of the molecule, i.e., C_2H_5 is the noninteracting site, therefore the alignment of the wires will be preferred/inclined along the polar H and O atom of the molecule and will stack along with it (Figure 2f). The availability of comparatively less interacting atoms has generated less accumulation of the ZnO NWs in the solution as compared to H_2O . The presence of a long chain C_2H_5 group avoids the stacking on ZnO NWs in the solution and results in less agglomeration (Figure S2c–e, Supporting Information). Comparatively, less agglomeration in ethanol increases the depletion region width and the NW–NW junction resistance (Figure S2f, Supporting Information) which results in an increase in the photocurrent and fast recovery time (≈ 14 s) than water (Figure 2c,d). The PD device has shown the best response when ZnO NWs were dispersed in IPA solution. Although the number of interacting atoms in ethanol and IPA is the same but the position of interacting atoms in IPA gives it an edge to hinder the agglomeration. The presence of bulky CH_3 groups on both sides of the potential coordination atoms

of IPA acts as a separator to prevent the agglomeration of the ZnO NWs. The absence of another IPA molecule in the nearby vicinity of a single IPA molecule due to steric hindrance results in the monodispersion of ZnO NWs (Figure 2f). These monodispersed ZnO NWs lead to uniform coating between contact electrodes with an increase in outer surface area for effective chemisorption under the absence of a UV source (Figure S2f, Supporting Information). As a result, the PD device fabricated from IPA-dispersed ZnO NWs demonstrated the fastest recovery time (≈ 100 ms) with enhanced photocurrent. These results suggest that the PDs performance is not only dependent on the type of dispersion solvent but also greatly influenced by the dispersion behavior of ZnO NWs in the solvent which in turn is dependent on the molecular geometry, carbon-chain length, steric hindrance, and position of the coordination atoms of the solvent molecule. The schematic illustration of the ZnO interactions with different solvent molecules and their respective dispersion in all solvents are given in Figure 2f. Due to an exceptional recovery time and enhanced photocurrent of PD in IPA solvent, ZnO NWs dispersed in IPA solvent were utilized for investigating the effect of contact electrodes on PDs performance.

2.1.2. ZnO NW-Metal Interaction on Contact Resistance of ZnO NW UV PDs

Three PD devices were fabricated using three different contact electrodes, namely, Ag, Ti/Au, and Ag NWs/Ag-paste. The time-resolved photoresponse were measured for all three devices by exposing them to 365 nm UV light. As shown in Figure 3a, an abrupt increase in photocurrent value from 0.1 pA to 10 μ A with a very high $I_{\text{dark}}/I_{\text{light}}$ ratio of $\approx 5 \times 10^5$ was observed for all the devices. The rise and recovery time of the PD devices at 0.5 μ W cm $^{-2}$ intensity is shown in Figure 3b. All the PDs exhibited fast response (≈ 200 ms), but the recovery time for Ag and Ag NWs/Ag-paste electrode-based devices were faster (< 100 ms) than the Ti/Au electrode-based device (10 s). As shown in Figure 3c, all the ZnO NW photodetectors demonstrated rectifying behavior across the metal contact electrodes. In general, a Schottky barrier is formed when the metal electrode work function is larger than the electron affinity of the semiconductor. However, in the case of nanostructures, surface states and/or source metal-ZnO interface reactions also influence the barrier height. In addition, series of resistance between the contact electrodes such as contact resistance and channel resistance will influence the I -V characteristics and the recovery behavior. It has been reported that Ti/Au forms an ohmic contact with ZnO nanostructures,^[28] while Ag is expected to form Schottky contact.^[29] For devices having rectifying contacts, i.e., Schottky contacts, there exist large resistance barriers at the MS interface (large depletion width), and thus, electrons require larger energy to overcome the barrier (Figure 3d and equation 4). As discussed in Figure 2a, the enhancement of electron concentration in the channel under UV exposure lowers the depletion width. Consequently, there is decrease in the magnitude of R_{C1} and R_{C2} in the case of Ag electrode that decreases the overall contact resistance (Figure 3d). When UV light is turned off, the depletion region width again extends to initial value

which increases the potential barrier at the MS contacts and eventually increases the contact resistance (Equation (4)). This additional energy barrier in the case of Ag electrodes helps to achieve fast recovery of current by abrupt blocking of electrons at the MS interface. The fast-switching behavior of Ag NWs/Ag-paste-based PD devices when exposed to 365 nm UV light at 0.35 μ W cm $^{-2}$ intensity for 15 cycles (1 s “on” and 1 s “off”) is shown in Figure 3e (Video SV1 and Figure S2h, Supporting Information). The photocurrent value decreased with UV intensity (Figure S2g, Supporting Information) and the device revealed 0.05 μ A at 0.05 μ W cm $^{-2}$ intensity. In comparison with state-of-the-art ZnO NWs PDs, our device demonstrated superior switching behavior, as shown in Table 1, therefore, we utilized Ag NWs/Ag-paste as contact electrode to fabricate high-performance stretchable PDs.^[8a–8d,15,30]

2.1.3. ZnO NWs PDs Embedded inside Kirigami and Mogul-Patterned PDMS and their Stretching Characteristics

In our previous work, we found that a honeycomb-like pattern leads to omnidirectional stretchability up to 20% strain in nonstretchable inorganic materials, namely, IGZO and Au.^[14a] In a similar manner, we utilized a novel structural engineering approach to fabricate two types of stretchable PDs (Figure 1a,b): i) made of honeycomb-patterned ZnO NWs embedded inside the mogul-patterned PDMS substrate (named as PD1), and ii) kirigami-shaped PDMS substrate (named as PD2) to achieve stable device performance under harsh bending and stretching conditions. The PD1, inspired by mogul pattern (bump and valley architecture), consists of honeycomb-patterned ZnO NWs PD device (honeycomb ZnO NW as active channel and honeycomb Ag NWs/Ag-paste as contact electrode) embedded in the valley region of the PDMS and alongside bump regions were filled with hexagonal PDMS cells. A photomicrograph image of this bump and valley architecture of PD1 is shown in Figure 4a. From the magnified scanning electron microscope (SEM) image of Figure 4a, it is evident that the ZnO NWs were embedded inside the PDMS valley region. Alternatively, the hexagonal PDMS cells in the bump region of PD1 have been replaced with an empty space to achieve a kirigami pattern-inspired PD device (Figure 4b) named as PD2. The fabrication processes of stretchable PDs are described in the Experimental Section. The photoresponse characteristics under different stretching conditions varied from 0% to 100% strain for PD1 and from 0% to 125% strain for PD2 are shown in Figure 4c–h. All the devices were characterized after releasing the strain. The responsivity values were extracted from the time-resolved photoresponse curve (Figure 4e,h). In the case of PD1, the responsivity of the device decreases exponentially with an increase in the stretching strain (Figure 4e). In the previous report, the stress distribution on the surface of bump/valley structure on mogul-patterned elastomeric substrate was analyzed experimentally and by computer simulation, after coating the top surface with the metal layer.^[31] It was reported that, for 50% strain, the stress distribution on the valley region (10^6 Pa) is 10^4 times higher in comparison with the bump region (10^2 Pa). Accordingly, the ZnO NWs embedded inside the PDMS valley region

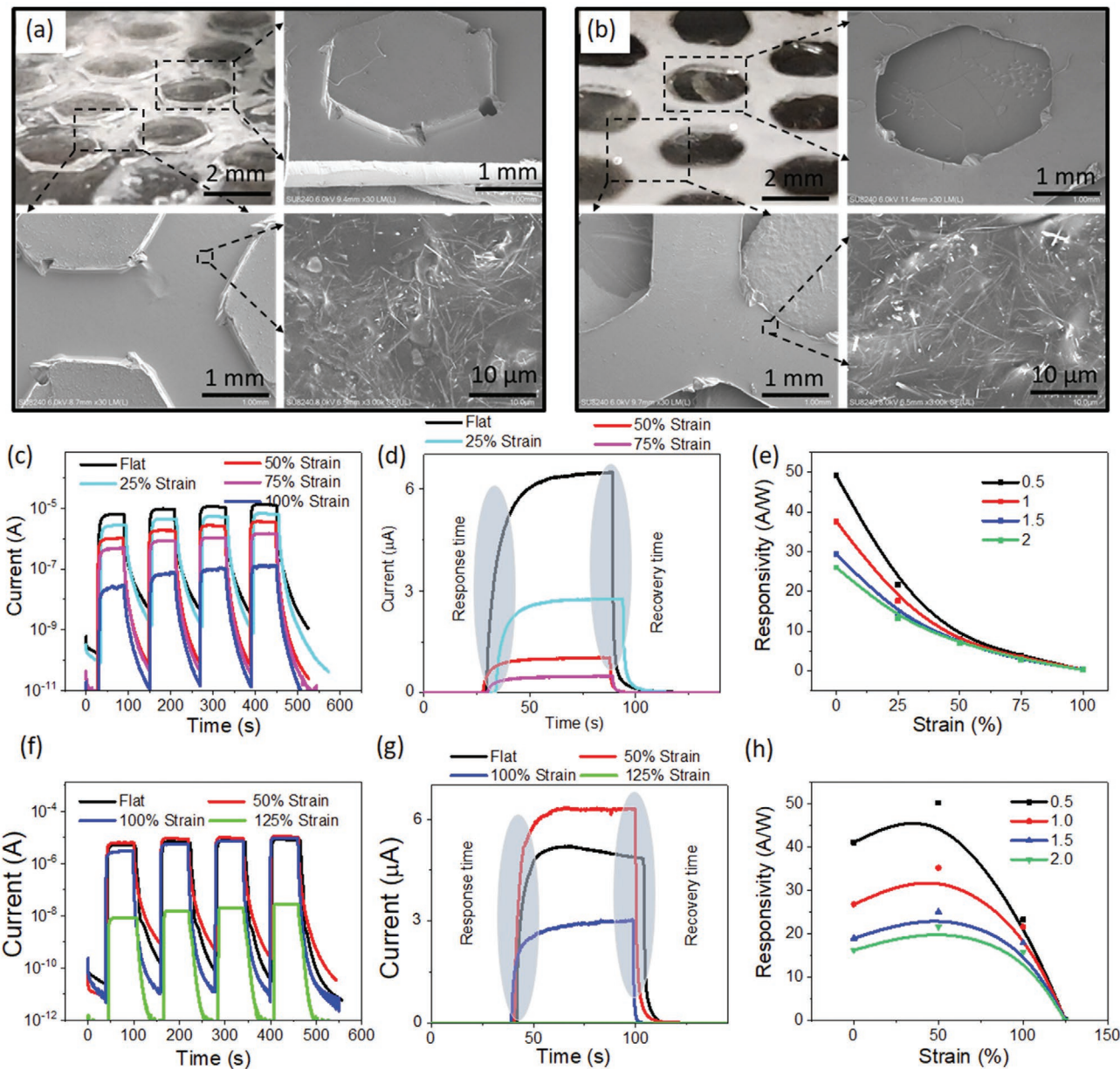


Figure 4. A photographic image and three magnified SEM images of honeycomb-patterned ZnO NW embedded in PDMS for a) the mogul-inspired pattern with bump and valley architecture (device-1) and b) the kirigami-inspired pattern with space in between honeycomb geometry (device-2). The device characteristics of device-1 and device-2 under various stretching: c–e) Photodetector characteristics of device-1 subjected to stretching up to 100% strain, c) time-dependent photoresponse, d) highlight the response and recovery characteristics, and e) the device responsivity; and f–h) photodetector characteristics of device-2 subjected to stretching up to 125% strain, f) time-dependent photoresponse, g) highlight the response and recovery characteristics, and h) the device responsivity.

experienced an increase in stress under stretching. It has been identified that the junction barrier due to the interaction of nanowires inside the PDMS matrix undergo three different conditions under stretching; 1) ohmic contact with low barrier height when the center lines of adjacent nanowires are in a distance less than the diameter of the nanowire itself; 2) tunneling effect when adjacent nanowires are in a distance greater than their diameter and less than the cut-off range; and 3) no connection when the distance of adjacent nanowires

is greater than cut-off range.^[32] Based on these conditions, the depletion barrier width increases when device subjected to the external stretching. Accordingly, the PD1 exhibited a decrease in photo-responsivity with respect to the stretching as shown in Figure 4e. On the contrary, PD2 demonstrated stable photocurrent value of $\approx 4.5 \mu\text{A}$ at $1 \mu\text{W cm}^{-2}$ UV intensity with negligible variation in responsivity ($\approx 20 \text{ A W}^{-1}$) up to 100% stretching (Figure 4f–h). This is because of the ability of kirigami-inspired pattern to accommodate the strain by

structural deformation which resulted in strain invariant electrical response.^[33] The induced stress value could be significantly reduced by introducing the hole in the bump region. It has been reported that the increase in the hole size decreases the induced stress value from GPa to kPa.^[34] The COMSOL simulation given in Figure S3 in the Supporting Information agrees with the previous observation that the surface stress of kirigami-patterned honeycomb PDMS is significantly low in comparison with the plain PDMS at 50% strain. In general, a nonlinear stress-strain behavior with three deformation regimes has been observed in the kirigami pattern: initial linear deformation regime, secondary elastic deformation, and finally the pattern collapse regime.^[33b] After the initial regime (<1% strain), the stress remains almost constant with negligible variation in the elastic deformation regime. Accordingly, based on our experimental observation, it is clearer that the PD2 revealed a nonlinear stress-strain behavior at elastic deformation regime with stable responsivity up to 100% strain. The photoresponse of PD2 measured under stretching is given in Figure S4 in the Supporting Information. The PD2 revealed a photo current value of >1 μA up to 100% strain (Video SV2, Supporting Information). It is worth mentioning that even at 125% strain, the PD2 exhibited the photocurrent ratio of >10⁵ and the responsivity of 66 mA W⁻¹ (Figure S4b,c, Supporting Information). At 125% strain, the honeycomb-patterned PDMS channel layer reaches its fracture limit resulting in permanent crack/tear as shown in Figure S4d in the Supporting Information. This decreased the active device area and eventually reduced the photocurrent value and the responsivity. In comparison with the previous reports (Table 1), the PD2 demonstrated an unprecedented stretchability (up to 125% strain) with stable photoresponse (up to 100% strain).^[8b,8c,14a,15] On the contrary, ZnO NW PD on plain PDMS suffered from complete failure at 50% strain with the photocurrent value of less than 1 nA (Figure S4g, Supporting Information). To demonstrate the reliability/robustness, the PD2 was subjected to cyclic stretching at 50% strain under UV illumination and photocurrent value was plotted. As shown in Figure 5a, the PD2 exhibited a stable variation in the photocurrent value under cyclic stretching and releasing up to 200 cycles. In addition, bending tests were performed on PD2. The time-dependent photoresponse and responsivity of the device, after subjecting to different bending radii varying from flat to less than 1 mm (\approx 150 μm) radius, are shown in Figure S4e,f in the Supporting Information. Similarly, the cyclic test was conducted by bending the device down to \approx 150 μm bending radius as shown in Figure 5b,c. The PD2 revealed stable device performance, a high $I_{\text{dark}}/I_{\text{light}}$ ratio of \approx 5 × 10⁵ at 0.5 μW cm⁻² UV intensity (365 nm), up to 1000 cycles at \approx 150 μm bending radius. The ZnO NWs has been long studied for their piezoelectric property for mechanical energy harvesting. Therefore, piezoresponse of our PDs was measured to quantify the piezoelectric output during stretching (see Figure S4h,i, Supporting Information). No significant electric output was observed from these experiments. In fact, this is expected, as in the present work, the laterally integrated ZnO NW-network is realized through randomly c-axis-oriented NWs inside a polymer matrix which may result in cancellation of the generated charges with negligible output

current and voltage (because the polarity of the induced piezo-potential inside individual NW are likely to cancel out each other). Thus, we can rule out the possibility of any significant contribution from the piezoelectric effect on photocurrent during stretching experiments. Based on the comparison with the state-of-the-art devices, the presented PD shows superior properties such as a high stretchability (125%) and excellent performance (Figure 5d),^[8b,8c,15,16,24a,35] making it an ideal candidate for wearable applications.

2.2. Flexible Triboelectric Nanogenerator (TENG) and its Characterizations

Flexible/stretchable self-powered smart sensors are key to the development of wearable technologies for applications such as next-generation soft robotics,^[36] human-machine interface,^[12b] etc. In this regard, the advances in TENGs-based energy harvesting are worth noting as they give a unique way of generating a high-voltage and low-current power supply, suitable for low-powered sensors such as PDs.^[7a,22a,22c,37] Herein, we have developed a flexible TENGs to power the stretchable PDs. The TENG device structure, functional characterization results, and its operating mechanism are shown in Figure 6. The schematic diagram of the TENG structure is shown in Figure 6a. The PDMS film serves as the negative triboelectric layer (top tribo-layer), and a polyethylene terephthalate (PET) sheet as a positive triboelectric layer (bottom tribo-layer). The electrodes are made of indium tin oxide (ITO). The primary function of the electrode is to couple electrostatically with the surface triboelectric charges and connect to the load via interface circuit. The working mechanism of the TENG under pressing/releasing cycle using mechanical shaker is shown in Figure 6b. In the experiment, a 2.5 × 2.5 cm² TENG device is used. As shown in Figure 6b-i, in the initial state, the surfaces of the two triboelectric materials are separated with a 2 mm distance (d) and have no triboelectric charges available to pump the electrons across the external load resistance “ R .” When a pressing force is applied using a mechanical shaker, the two triboelectric layers contact each other and equal amounts of positive and negative charges on the contact surface are generated (Figure 6b-ii). This charge generation phenomenon can be understood by their ability to gain or lose electrons, which relies on their varied tribo-polarity.^[22c,37a] Once the pressing force is released, the two triboelectric layers move away from each other, and this will drive electrons through the external circuit to balance the potential difference between two electrodes attached on the back of triboelectric layers (Figure 6b-iii). Thus, the voltage and current signals can be obtained in the external load circuit. The output performance (output voltage and current) for a typical TENG at 8 N compressive force for various operating frequencies across 1 MΩ resistance are shown in Figure 6c,d. The low frequency range (2–10 Hz) is selected for these experiments as it is the typical vibrational frequency range present in our day-to-day life environment such as while walking, body movements, etc. As shown in Figure 6c, at 2 Hz, the peak output voltage generated by the TENG was \approx 34 V. As the applied frequency increased from 2 to 10 Hz, the peak output voltage increased, and reached a maximum

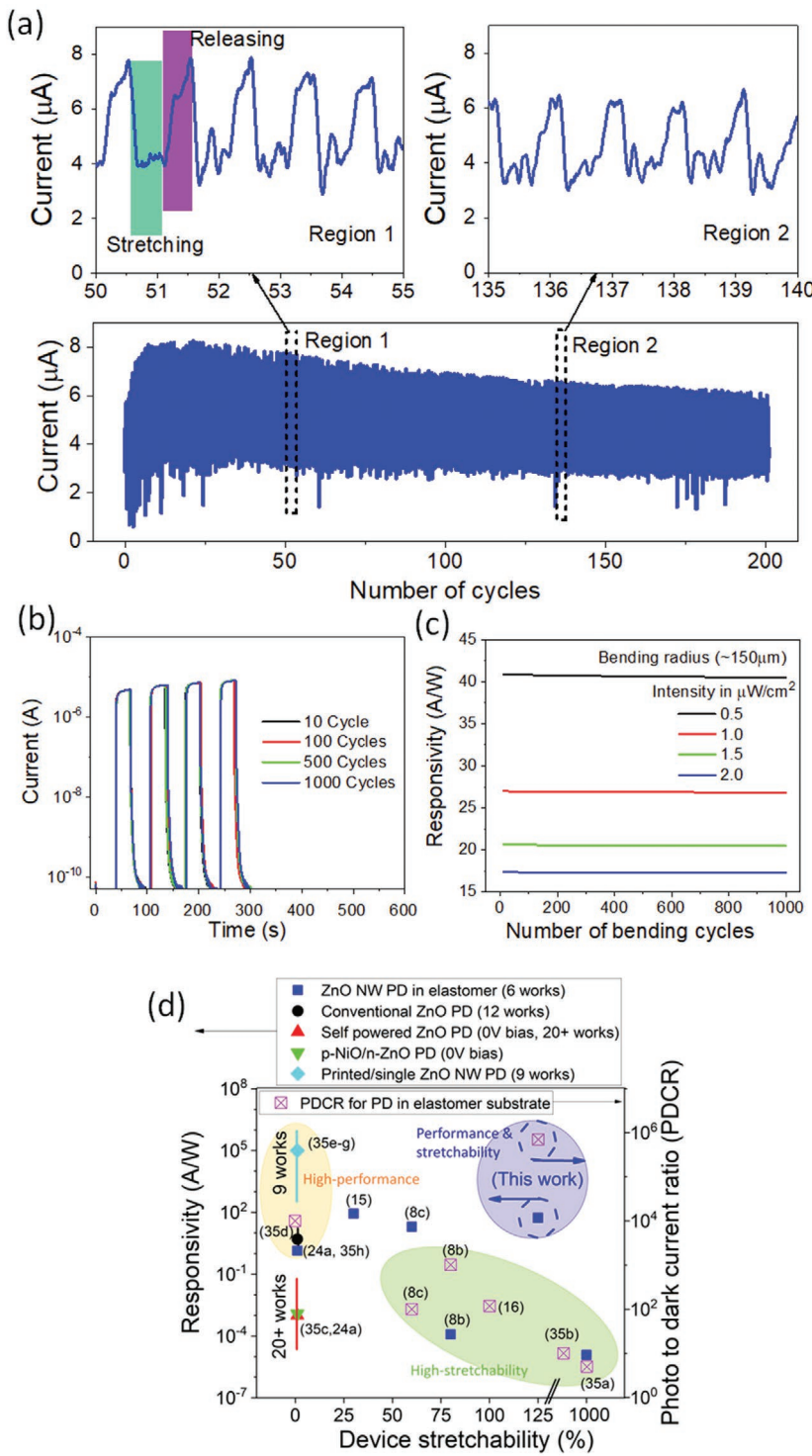


Figure 5. Device reliability test: a) Cyclic stretching and releasing up to 200 cycles at 50% strain under UV illumination and their magnified graphs at two different region such as region 1 between 50 and 55 cycles and region 2 between 135 and 140 cycles; and b) sensing response at $\approx 150 \mu\text{m}$ bending radius for 1000 bending cycles and c) their responsivity. d) Comparison of our current work with the state-of-the-art ZnO PDs.

value of ≈ 75 V. Further, the peak output current increases from ≈ 4 to $\approx 17 \mu\text{A}$ with the increase in applied frequency (Figure 6d). The enhancement in the TENG output performance with the increasing frequency could be explained by the faster transfer

of the free charges.^[38] Energy harvesting devices present an internal impedance to the connected external load and in general, the maximum output power could be delivered when the load impedance is matched to that of the energy harvester.

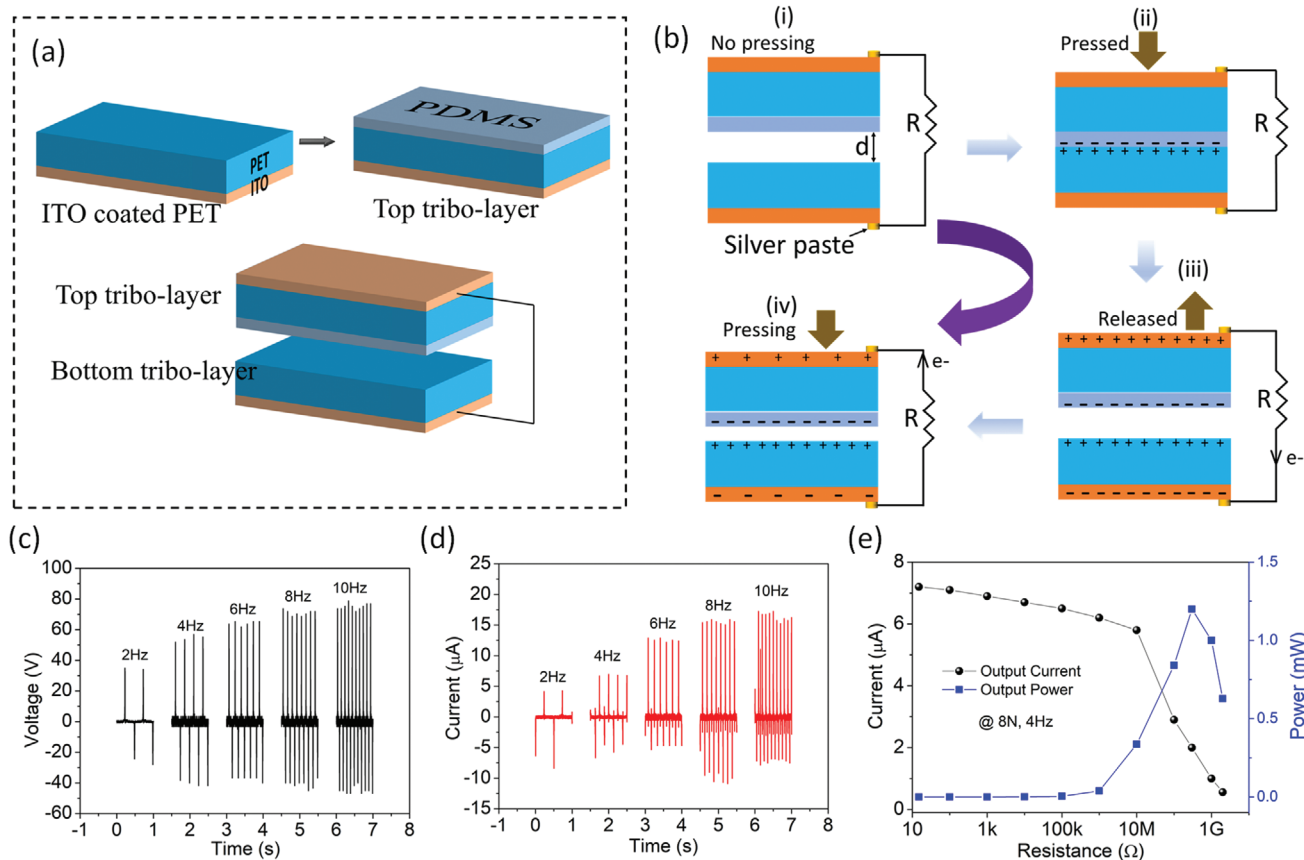


Figure 6. a) Schematic of the TENG device structure, b) schematic showing the TENG device working mechanism. c–e) Functional characterization results of the fabricated TENG devices at 8 N compressive force: c) output voltage as a function of frequency across $1\text{ M}\Omega$, d) output current as a function of frequency across $1\text{ M}\Omega$, and e) peak output current amplitude and output instantaneous peak power as a function of load resistance at 4 Hz.

Therefore, the optimal output power was assessed by measuring the output current across the wide range of resistive loads ($15\text{--}2\text{G }\Omega$) by applying 8 N force at 4 Hz. The maximum instantaneous output power (P_{ins}) is given by $P_{\text{ins}} = I^2 R_L$ where I is the instantaneous output current across the resistance R_L . Figure 6e shows a data graph for the peak output current and peak output power against resistive loads. As expected, as the load resistance increases, the amplitude of the peak output current starts to decrease. Using the P_{ins} equation, a typical bell-shaped output power curve as a function of resistive load is obtained. Correspondingly, the peak output power reaches a maximum value of 1.2 mW at an optimal load of $300\text{ M}\Omega$. The maximum power is obtained when the distance between the two triboelectric layers, i.e., d is maximum. When the two triboelectric layers are approaching on applying pressing forces, the electrons in the opposite direction will flow in the external circuit until the two layers fully contact each other (Figure 6b-iv). This explains the AC-type voltage and current output from our TENG devices during periodic pressing. The device flexibility/stability was tested by bending the device (both convex and concave) and measuring it under identical conditions before and after bending (Figure S5, Supporting Information). The obtained results showed the exceptional flexibility of the TENG device which is needed for wearable applications.

2.3. Integration of Stretchable Photodetector with TENG

In this section, we will demonstrate the concept of energy autonomous UV photodetection. Before the demo, the high flexibility/conformability of the fabricated stretchable photodetector was tested by placing it over human fingers under flat and bending conditions (Figure S6a, Supporting Information). This confirms the suitability of fabricated devices for wearable applications. In fact, the developed contact-separation TENGs would be ideally placed within the shoe as insole to harvest biomechanical energy. The stepping motion during walking results in the contact/separation of vertically stacked two contact layers. Using such an integration strategy, generation of a high output electric signal for each step has been successfully demonstrated in the past.^[39] In our work, the proposed TENG generated enough power with stepping motion and tapping motion as shown in Figure S6b in the Supporting Information (Video SV3, Supporting Information). Following that, the TENG output voltage was measured across PD2 at 8 N compressive force for various operating frequencies. It is to note that these measurements were performed with and without UV radiation to ensure the continuous working of PD2 under UV exposure. As shown in Figure 7a, under both conditions, the peak output voltage increases with the increase in the applied frequency. It is also interesting to note that the

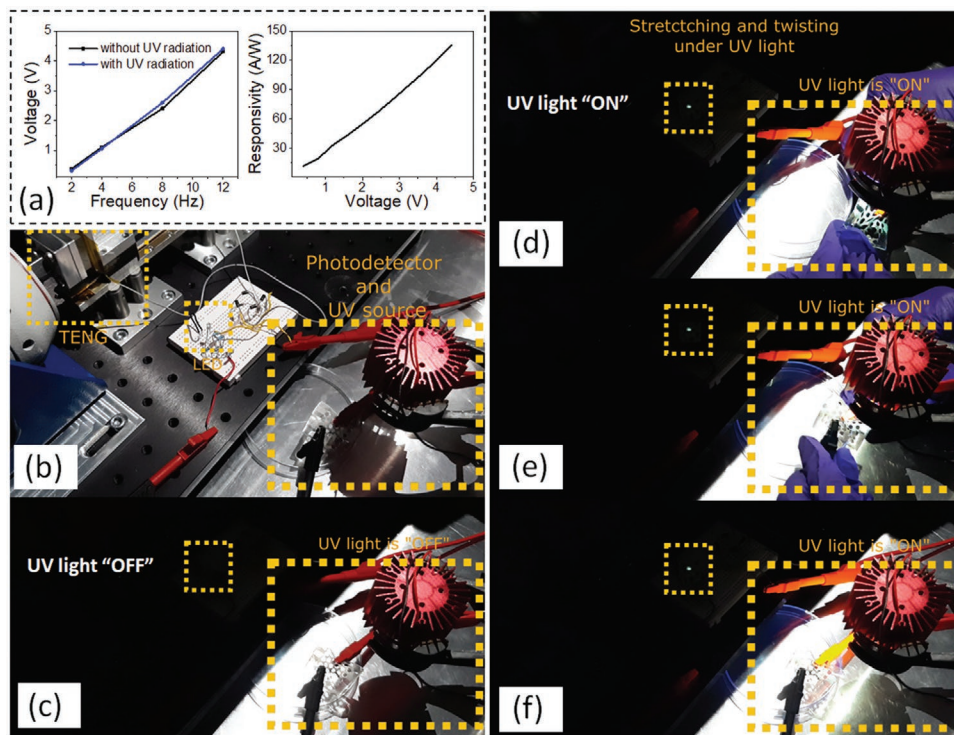


Figure 7. Integration of stretchable PD with TENG: a) Output voltage of TENG at different frequency across PD irradiated with and without UV light and their respective responsivity at generated voltage. Photographic demo showing the connection of LED in series with self-powered photodetector for real-time UV detection; b) experimental setup; c) UV radiation is OFF and the LED in the circuit is OFF; d) UV source is turned ON and the LED glows; and e,f) the real-time status of LED under harsh stretching and twisting.

output voltage under UV exposure does not decrease and enough to drive the PD2. To elucidate the effect of applied voltage on PD performance, responsivity versus voltage curve is also shown in Figure 7a. The presented data show that the driving voltage for PD2 could be as low as 0.5 V. Accordingly, a self-powered UV PD concept was implemented by integrating PD2 with the TENG through a rectifier bridge circuit and operated by applying 8 N force at 4 Hz. A light-emitting diode (LED) was connected in series with the PD2, in other words, one terminal of PD2 was connected to TENG through the bridge rectifier circuit and another end was connected to the LED light. The setup and the working demo of self-powered PD are given in Figure 7 (Video SV4, Supporting Information). Without UV radiation, the resistance of the UV detector remains high so there is no current flow. As a result, the LED was in an “off” state (Figure 7c). When PD2 was exposed to UV radiation, the resistance of the PD decreased, allowing the current to flow through the PD and hence LED started glowing, as shown in Figure 7d. Further, the harsh deformations (stretching, bending, and twisting) do not affect the ability of PD to detect the UV radiation (Figure 7e,f). Thus, the presented self-powered stretchable PD can be attached to any curvilinear surfaces, such as fabric and skin, for real-time detection of UV radiation for health and environmental monitoring.

3. Conclusion

In conclusion, the extremely stretchable high-performance ZnO NWs PD integrated with flexible TENGs for real-time UV

detection was demonstrated. The PD with high-performance and extreme stretchability has been achieved by optimizing three parameters, namely, dispersion solvent, contact electrodes, and structural engineering of the substrate. The PD device fabricated using IPA dispersed ZnO NWs, and Ag NWs/Ag-paste-based electrode revealed excellent sensor performance with fast response time of ≈ 200 ms and recovery time of <100 ms, and a high I_{dark}/I_{light} ratio of $\approx 5 \times 10^5$. Further, embedding such device inside kirigami-patterned PDMS substrate in honeycomb geometry demonstrates an unprecedented stretchability up to 125% strain without any performance degradation with the high responsivity of ≈ 54 A W $^{-1}$. The stretchable PD integrated with flexible TENG demonstrated the possibility of real-time UV radiation monitoring through observing the light intensity of the LED.

4. Experimental Section

Figure 1 depicts the fabrication schematic of two types of stretchable PDs (kirigami and mogul pattern inspired devices), flexible TENG and integration of photodetector with TENG to demonstrate self-powered stretchable PD for real-time UV detection using LED light.

Fabrication of Stretchable ZnO NW Photodetector: The ZnO NWs with length and width of ≈ 20 μ m and ≈ 50 nm were purchased from Novarials Corporation (NovaWire- ZnO-A50). Stretchable PD devices were fabricated by two-step processes that include fabrication of PD device, by drop-casting ZnO-NW channel and Ag-NW contact electrodes, on patterned PVC substrate and transfer to kirigami- and mogul-inspired PDMS as embedded architecture. Figure 1a shows, the first step, the fabrication of ZnO NWs PD on honeycomb-patterned

PVC substrate. A honeycomb-pattern with the line width of 1.2 mm, the line length of 2.5 mm, the length along the armchair direction of 5 mm, and length along the zigzag direction of 4.3 mm over a 2.5 cm x 2.5 cm area was realized on \approx 175 μ m thick PVC sheet using a computer-controlled blade cutter (Silhouette Cameo) tool. The Ag NW solution was drop-casted over the entire substrate and wiped-off using cotton buds to define the channel width and length of 4 mm and 1.1 cm, which defined the active device area of \approx 24 mm² (Figure S7, Supporting Information). Sequentially, ZnO NW solution was drop-casted over the entire substrate and the Ag-Paste was applied gently on top of Ag NWs contact electrode region to achieve good contact. Figure 1b shows the second step of the stretchable PD fabrication process which included embedding the PD into mogul or kirigami-patterned PDMS substrate to achieve PD1 (mogul-pattered device) and PD2 (kirigami-patterned device), respectively. In the case of PD1 (Figure 1b-i), the PDMS elastomer and curing agent mixing ratio of 10:1 was drop-casted over the entire 2.5 cm x 2.5 cm area and cured at 60 °C for 2 h. Sequentially, the PDMS with the embedded ZnO NWs PD device was peeled-off from PVC to obtain bump and valley architecture in which the bump region contained a thick PDMS layer and honeycomb valley region contained embedded ZnO NWs PD (Figure 4a). In the case of PD2 (Figure 1b,c-ii), the PDMS was carefully casted over the PVC/device region without covering the honeycomb openings and cured at 60 °C for 2 h. Thereby, after peel-off from PVC, the honeycomb ZnO NWs PD was embedded inside the honeycomb PDMS, leaving hexagonal gaps to obtain a kirigami-inspired pattern. The SEM image of mogul- and kirigami-inspired architecture is shown in Figure 4a,b, respectively.

Self-Powered Stretchable Photodetector: Self-powered stretchable PD was realized by coupling the TENG with PD for real-time UV detection. Figure 6a shows the schematic of the fabrication process of flexible TENG which was consisted of ITO as top and bottom contacts, PET as a positive dielectric layer, and PDMS as a negative dielectric layer.^[22c] A commercially available ITO-coated PET sheet of 2 cm x 2 cm was used as the bottom half of TENG. The top half of the TENG layer was fabricated by spin-coating \approx 20 μ m thick PDMS on the PET side of the ITO-coated PET substrate. Finally, the device was assembled by placing the top half of the TENG layer with the bottom half of the TENG with a layer of Kapton tape separating both the layers for sufficient isolation as shown in Figure 6a. Sequentially, the TENG was coupled with stretchable PD via LED light for real-time monitoring of UV radiation through the status of LED as shown in Figure 1c.

Statistics: The SEM images were attained using FEI Nova NanoSEM. The electrical measurements of PDs such as time-resolved photoresponse and I-V characteristics were measured using semiautomated summit 12k Auto prober and semiconductor device parameter analyzer. Stretching and bending tests were carried out using custom-made system consisted of two linear stage motor (VT-21 from Micronic USA) connected to the Pollux Box driven by Labview software precisely control the stage movement. A TIRA shaker was used to supply mechanical pressing force to the TENG and an oscilloscope (KETSIGHT, MSO-X 4154A) and/or digital multimeter (KEYSIGHT, 3446X) were used to record the output current and voltage of TENG.

Supporting Information

Supporting Information is available from the Wiley Online Library or from the author.

Acknowledgements

This work was supported in part bys Engineering and Physical Sciences Research Council (EPSRC) through engineering fellowship for growth (EP/R029644/1) and Programme Grant – Heteroprint (EP/R03480X/1) and European Commission through FET-OPEN project Ph-Coding (H2020-FETOPEN-2018- 829186).

Conflict of Interest

The authors declare no conflict of interest.

Data Availability Statement

Research data are not shared.

Keywords

mogul and kirigami structures, photodetectors, stretchable electronics, structural engineering, triboelectric nanogenerators

Received: July 5, 2021

Revised: August 11, 2021

Published online: September 4, 2021

- [1] a) H. Chen, K. Liu, L. Hu, A. A. Al-Ghamdi, X. Fang, *Mater. Today* **2015**, *18*, 493; b) T. A. Kalajian, A. Aldoukh, A. J. Veronikis, K. Persons, M. F. Holick, *Sci. Rep.* **2017**, *7*, 11489.
- [2] E. Boyes, M. Stanisstreet, *J. Environ. Educ.* **1998**, *29*, 31.
- [3] I. V. Ivanov, T. Mappes, P. Schaupp, C. Lappe, S. Wahl, *J. Biophotonics* **2018**, *11*, 201700377.
- [4] a) D. Mohania, S. Chandel, P. Kumar, V. Verma, K. Digvijay, D. Tripathi, K. Choudhury, S. K. Mitten, D. Shah, in *Ultraviolet Light in Human Health, Diseases and Environment* (Ed: S. I. Ahmad), Springer International Publishing, Cham **2017**, p. 71; b) S. J. Park, H. K. Yang, B. K. Moon, *Nano Energy* **2019**, *60*, 87.
- [5] M. Burtscher, *Aging Dis.* **2013**, *5*, 274.
- [6] a) A. Prakash, S. D. Nehate, K. B. Sundaram, *Opt. Express* **2016**, *41*, 4249; b) X. Wang, W. Song, B. Liu, G. Chen, D. Chen, C. Zhou, G. Shen, *Adv. Funct. Mater.* **2013**, *23*, 1202.
- [7] a) Y. Zhang, M. Peng, Y. Liu, T. Zhang, Q. Zhu, H. Lei, S. Liu, Y. Tao, L. Li, Z. Wen, X. Sun, *ACS Appl. Mater. Interfaces* **2020**, *12*, 19384; b) C. García Núñez, L. Manjakkal, R. Dahiya, *npj Flexible Electron.* **2019**, *3*, 1.
- [8] a) L. Meng, G. Li, X. Tian, S. Bai, Q. Xu, X. Jia, X. Cui, Y. Qin, W. Wu, *ACS Appl. Mater. Interfaces* **2020**, *12*, 1054; b) J. Kim, H. Park, S.-H. Jeong, *J. Ind. Eng. Chem.* **2020**, *82*, 144; c) D.-H. Lien, H.-P. Wang, S.-B. Chen, Y.-C. Chi, C.-L. Wu, G.-R. Lin, Y.-C. Liao, J.-H. He, *npj Flexible Electron.* **2018**, *2*, 19; d) C. G. Núñez, A. Vilouras, W. T. Navaraj, F. Liu, R. Dahiya, *IEEE Sens. J.* **2018**, *18*, 7881; e) J. Han, J. Lee, S. Ju, *AIP Adv.* **2016**, *6*, 045218; f) C. García Núñez, F. Liu, W. T. Navaraj, A. Christou, D. Shakthivel, R. Dahiya, *Microsyst. Nanoeng.* **2018**, *4*, 22; g) T. Q. Trung, N.-E. Lee, *Adv. Mater.* **2017**, *29*, 1603167.
- [9] a) W. Dang, V. Vinciguerra, L. Lorenzelli, R. Dahiya, *Flexible Printed Electron.* **2017**, *2*, 013003; b) Y. Kumaresan, N. Yogeswaran, L. Occhipinti, R. Dahiya, *Stretchable Systems: Materials, Technologies, and Applications*, Cambridge University Press, Cambridge **2021**.
- [10] a) J. Kim, I. Jeerapan, S. Imani, T. N. Cho, A. Bandodkar, S. Cinti, P. P. Mercier, J. Wang, *ACS Sens.* **2016**, *1*, 1011; b) J. Choi, R. Ghaffari, L. B. Baker, J. A. Rogers, *Sci. Adv.* **2018**, *4*, eaar3921; c) P. Escobedo, M. Bhattacharjee, F. Nikbakhtnasrabad, R. Dahiya, *IEEE Internet Things J.* **2021**, *8*, 5093; d) Y. Wang, Y. Qiu, S. K. Ameri, H. Jang, Z. Dai, Y. Huang, N. Lu, *npj Flexible Electron.* **2018**, *2*, 6.
- [11] O. Ozioko, P. Karipoth, M. Hersh, R. Dahiya, *IEEE Trans. Neural Syst. Rehabil. Eng.* **2020**, *28*, 1344.
- [12] a) O. Ozioko, P. Karipoth, P. Escobedo, M. Ntagios, A. Pullanchiyodan, R. Dahiya, *Adv. Intell. Syst.* **2021**, *3*, 1900145; b) R. Dahiya, N. Yogeswaran, F. Liu, L. Manjakkal, E. Burdet, V. Hayward, H. Jörntell, *Proc. IEEE* **2019**, *107*, 2016.

- [13] A. Pullanchiyodan, L. Manjakkal, S. Dervin, D. Shakthivel, R. Dahiya, *Adv. Mater. Technol.* **2020**, *5*, 1901107.
- [14] a) Y. Kumaresan, H. Kim, Y. Pak, P. K. Poola, R. Lee, N. Lim, H. C. Ko, G. Y. Jung, R. Dahiya, *Adv. Electron. Mater.* **2020**, *6*, 2000058; b) M. Bhattacharjee, M. Soni, P. Escobedo, R. Dahiya, *Adv. Electron. Mater.* **2020**, *6*, 2000445.
- [15] T. Q. Trung, V. Q. Dang, H.-B. Lee, D.-I. Kim, S. Moon, N.-E. Lee, H. Lee, *ACS Appl. Mater. Interfaces* **2017**, *9*, 35958.
- [16] C. Yan, J. Wang, X. Wang, W. Kang, M. Cui, C. Y. Foo, P. S. Lee, *Adv. Mater.* **2014**, *26*, 943.
- [17] C.-W. Chiang, G. Haider, W.-C. Tan, Y.-R. Liou, Y.-C. Lai, R. Ravindranath, H.-T. Chang, Y.-F. Chen, *ACS Appl. Mater. Interfaces* **2016**, *8*, 466.
- [18] G. Lee, S. G. Lee, Y. Chung, G. Y. Bae, S. Lee, S. Ryu, K. Cho, *Adv. Electron. Mater.* **2016**, *2*, 1600158.
- [19] a) S. Dhar, T. Majumder, S. P. Mondal, *ACS Appl. Mater. Interfaces* **2016**, *8*, 31822; b) L. Yang, W.-L. Tsai, C.-S. Li, B.-W. Hsu, C.-Y. Chen, C.-I. Wu, H.-W. Lin, *ACS Appl. Mater. Interfaces* **2019**, *11*, 47054.
- [20] a) O. Game, U. Singh, T. Kumari, A. Banpurkar, S. Ogale, *Nanoscale* **2014**, *6*, 503; b) Z. Chen, Z. Cheng, J. Wang, X. Wan, C. Shu, H. K. Tsang, H. P. Ho, J.-B. Xu, *Adv. Opt. Mater.* **2015**, *3*, 1207.
- [21] E. Butanovs, S. Vlassov, A. Kuzmin, S. Piskunov, J. Butikova, B. Polyakov, *ACS Appl. Mater. Interfaces* **2018**, *10*, 13869.
- [22] a) Z. Wen, J. Fu, L. Han, Y. Liu, M. Peng, L. Zheng, Y. Zhu, X. Sun, Y. Zi, *J. Mater. Chem. C* **2018**, *6*, 11893; b) C.-H. Lin, H.-C. Fu, D.-H. Lien, C.-Y. Hsu, J.-H. He, *Nano Energy* **2018**, *51*, 294; c) G. Min, L. Manjakkal, D. M. Mulvihill, R. Dahiya, *IEEE Sens. J.* **2020**, *20*, 6856.
- [23] a) D. Tomer, S. Rajput, L. J. Hud, C. H. Li, L. Li, *Appl. Phys. Lett.* **2014**, *105*, 021607; b) F. Yang, M. Zheng, L. Zhao, J. Guo, B. Zhang, G. Gu, G. Cheng, Z. Du, *Nano Energy* **2019**, *60*, 680.
- [24] a) B. D. Boruah, *Nanoscale Adv.* **2019**, *1*, 2059; b) Y. Liu, X. Zhang, J. Su, H. Li, Q. Zhang, Y. Gao, *Opt. Express* **2014**, *22*, 30148.
- [25] S. M. Sze, K. K. Ng, in *Physics of Semiconductor Devices*, Wiley, New York **2006**, p. 134.
- [26] A. Ejaz, J. H. Han, R. Dahiya, *J. Colloid Interface Sci.* **2020**, *570*, 322.
- [27] a) S. Carapezzi, G. Priante, V. Grillo, L. Montès, S. Rubini, A. Cavallini, *ACS Nano* **2014**, *8*, 8932; b) Y. Kumaresan, R. Lee, N. Lim, Y. Pak, H. Kim, W. Kim, G. Y. Jung, *Adv. Electron. Mater.* **2018**, *4*, 1800167; c) S. Chakraborty, J. Chattopadhyay, H. Peng, Z. Chen, A. Mukherjee, R. S. Arvidson, R. H. Hauge, W. E. Billups, *J. Phys. Chem. B* **2006**, *110*, 24812; d) J. Hou, M. Yang, C. Ke, G. Wei, J. Zhang, *Nanoscale* **2020**, *12*, 13858.
- [28] A. S. Dahiya, C. Opoku, C. Oshman, G. Poulin-Vittrant, F. Cayrel, L. P. Tran Huu Hue, D. Alquier, N. Camara, *Appl. Phys. Lett.* **2015**, *107*, 033105.
- [29] L. Wen, K. M. Wong, Y. Fang, M. Wu, Y. Lei, *J. Mater. Chem.* **2011**, *21*, 7090.
- [30] a) S. Bai, W. Wu, Y. Qin, N. Cui, D. J. Bayerl, X. Wang, *Adv. Funct. Mater.* **2011**, *21*, 4464; b) Y. Li, Y. Li, J. Chen, Z. Sun, Z. Li, X. Han, P. Li, X. Lin, R. Liu, Y. Ma, W. Huang, *J. Mater. Chem. C* **2018**, *6*, 11666.
- [31] H.-B. Lee, C.-W. Bae, L. T. Duy, I.-Y. Sohn, D.-I. Kim, Y.-J. Song, Y.-J. Kim, N.-E. Lee, *Adv. Mater.* **2016**, *28*, 3069.
- [32] M. Amjadi, A. Pichitpajongkit, S. Lee, S. Ryu, I. Park, *ACS Nano* **2014**, *8*, 5154.
- [33] a) M. Isobe, K. Okumura, *J. Phys. Soc. Japan* **2019**, *88*, 025001; b) M. Isobe, K. Okumura, *Sci. Rep.* **2016**, *6*, 24758; c) T. C. Shyu, P. F. Damasceno, P. M. Dodd, A. Lamoureux, L. Xu, M. Shlian, M. Shtein, S. C. Glotzer, N. A. Kotov, *Nat. Mater.* **2015**, *14*, 785.
- [34] T. Takahashi, K. Takei, A. G. Gillies, R. S. Fearing, A. Javey, *Nano Lett.* **2011**, *11*, 5408.
- [35] a) C.-H. Lin, D.-S. Tsai, T.-C. Wei, D.-H. Lien, J.-J. Ke, C.-H. Su, J.-Y. Sun, Y.-C. Liao, J.-H. He, *ACS Nano* **2017**, *11*, 10230; b) X. Xu, Y. Zuo, S. Cai, X. Tao, Z. Zhang, X. Zhou, S. He, X. Fang, H. Peng, *J. Mater. Chem. C* **2018**, *6*, 4866; c) Z. Chen, B. Li, X. Mo, S. Li, J. Wen, H. Lei, Z. Zhu, G. Yang, P. Gui, F. Yao, G. Fang, *Appl. Phys. Lett.* **2017**, *110*, 123504; d) S. Wang, Y. Zou, Q. Shan, J. Xue, Y. Dong, Y. Gu, J. Song, *RSC Adv.* **2018**, *8*, 33666; e) X. Liu, L. Gu, Q. Zhang, J. Wu, Y. Long, Z. Fan, *Nat. Commun.* **2014**, *5*, 4007; f) J. Long, W. Xiong, C. Wei, C. Lu, R. Wang, C. Deng, H. Liu, X. Fan, B. Jiao, S. Gao, L. Deng, *Nano Lett.* **2020**, *20*, 5159; g) T. Chen, X. Gao, J.-Y. Zhang, J.-L. Xu, S.-D. Wang, *Adv. Opt. Mater.* **2020**, *8*, 1901289; h) B. D. Boruah, A. Mukherjee, A. Misra, *Nanotechnology* **2016**, *27*, 095205.
- [36] a) J. Chen, B. Chen, K. Han, W. Tang, Z. L. Wang, *Adv. Mater. Technol.* **2019**, *4*, 1900337; b) L. Manjakkal, W. T. Navaraj, C. G. Núñez, R. Dahiya, *Adv. Sci.* **2019**, *6*, 1802251.
- [37] a) Y. Xu, G. Min, N. Gadegaard, R. Dahiya, D. M. Mulvihill, *Nano Energy* **2020**, *76*, 105067; b) G. Min, Y. Xu, P. Cochran, N. Gadegaard, D. M. Mulvihill, R. Dahiya, *Nano Energy* **2021**, *83*, 105829.
- [38] Y. Xie, S. Wang, S. Niu, L. Lin, Q. Jing, J. Yang, Z. Wu, Z. L. Wang, *Adv. Mater.* **2014**, *26*, 6599.
- [39] a) S. Li, J. Wang, W. Peng, L. Lin, Y. Zi, S. Wang, G. Zhang, Z. L. Wang, *Adv. Energy Mater.* **2017**, *7*, 1602832; b) G. Q. Gu, C. B. Han, J. J. Tian, C. X. Lu, C. He, T. Jiang, Z. Li, Z. L. Wang, *ACS Appl. Mater. Interfaces* **2017**, *9*, 11882; c) G. Zhu, P. Bai, J. Chen, Z. Lin Wang, *Nano Energy* **2013**, *2*, 688.